Photometric properties of reionization-epoch galaxies in the SIMBA simulations

Xiaohan Wu ®,[1]★ Romeel Davé ®,[2,3,4]★ Sandro Tacchella ®[1] and Jennifer Lotz[5]

[1]*Center for Astrophysics – Harvard and Smithsonian, 60 Garden St, Cambridge, MA 02138, USA*
[2]*Institute for Astronomy, University of Edinburgh, Edinburgh EH9 3HJ, UK*
[3]*University of the Western Cape, Bellville, Cape Town 7535, South Africa*
[4]*South African Astronomical Observatories, Observatory, Cape Town 7925, South Africa*
[5]*Space Telescope Science Institute, 3700 San Martin Drive, Baltimore, MD 21218, USA*

ABSTRACT

We study the photometric properties and sizes of the reionization-epoch galaxies in high-resolution SIMBA cosmological hydrodynamical simulations with box sizes of $[25, 50]\,h^{-1}$ Mpc. Assuming various attenuation laws, we compute photometry by extincting each star particle's spectrum using the line-of-sight gas metal column density. The predicted ultraviolet luminosity function (UVLF) generally agrees with observations at $z = 6$, owing to a partial cancellation between the high metallicities of the simulated galaxies and lower dust-to-metal ratios. The simulated $z = 8$ UVLF is low compared to observations, likely owing to excessive dust extinction. SIMBA predicts UV continuum slopes (β) in agreement with the $z = 6$ observations, with the best agreement obtained using a Calzetti extinction law. Interestingly, the gas-phase mass–metallicity relation in SIMBA is higher at $z \sim 6$ than at $z \sim 2$, suggesting that rapid early enrichment (and dust growth) might be necessary to match the observed β. We find that β is more sensitive to the dust extinction law than the UVLF. By generating mock *James Webb Space Telescope* (*JWST*) images and analysing in a manner similar to observations, we show that SIMBA's galaxy size–luminosity relation well reproduces the current $z = 6$ *Hubble* observations. Unlike observations at lower redshifts, SIMBA predicts similar rest-UV and rest-optical sizes of $z = 6$ galaxies, owing to weak age gradients and dust extinction in star-forming regions counteract each other to weaken the colour gradients within galaxies. These predictions will be testable with *JWST*.

Key words: galaxies: evolution – galaxies: formation – galaxies: high-redshift – galaxies: photometry – galaxies: stellar content.

1 INTRODUCTION

Our understanding of galaxy evolution over the first billion years after the big bang has been revolutionized since the installation of the Wide Field Camera 3 (WFC3) on board the *Hubble Space Telescope* (*HST*). The remarkable near-infrared (IR) capabilities of WFC3 has enabled more than 1000 galaxies to be detected at $6 < z < 10$, allowing a thorough investigation into star formation in the very early universe. This cosmic frontier will be pushed even more forward with the launch of the *James Webb Space Telescope* (*JWST*), with its unprecedented IR sensitivity and spatial resolution. The physical properties of these young galaxies provide direct tests of our theoretical picture of galaxy formation, where gas inflows, outflows, and other feedback processes shape the star formation

histories together. In addition, observations of these early objects shed light on whether their emergence provided enough ionizing photons to make reionization of the intergalactic medium (IGM) possible – the last major phase transition of the IGM (for a recent review, see Stark 2016).

One of the most fundamental measurements at $z \gtrsim 6$ is the galaxy rest-frame ultraviolet luminosity function (UVLF). The UVLF gives the volume density of galaxies as a function of their rest-UV luminosity, canonically parametrized by a Schechter (1976) function. Comparisons between the galaxy LF and the halo mass function provide insights into the physical processes that affect galaxy formation across cosmic time, for example supernova (SN) feedback which shapes the faint end of the LF (e.g. Somerville & Davé 2015). Moreover, observing the UVLF at $z \gtrsim 6$ probes the role of early galaxies in the epoch of reionization (EoR), owing to the correlation between the rest-frame UV luminosity and recent star formation activities for all but the most dust-obscured galaxies.

★ E-mail: xiaohan.wu@cfa.harvard.edu (XW); romeeld@gmail.com (RD)

The recent measurements of Bouwens et al. (2015) and Finkelstein et al. (2015) showed that the faint-end slope of the UVLF is steeper with increasing redshift, consistent with the evolution of the halo mass function (see also Tacchella, Trenti & Carollo 2013; Mason, Trenti & Treu 2015; Tacchella et al. 2018b). It reaches $\simeq -2$ by $z \simeq 7$–8 (but see also Bouwens et al. 2017; Livermore, Finkelstein & Lotz 2017; Atek et al. 2018), suggesting that low-luminosity galaxies dominate the integrated UV luminosity during reionization. Such a steep faint-end slope also implies that the ionizing photon budget produced by these early galaxies is sufficient to reionize the universe by $z \simeq 6$ with modest ionizing photon escape fractions (e.g. Robertson et al. 2013; Finkelstein et al. 2019; but see also Naidu et al. 2019).

While the UVLF gives the galaxy abundances, the UV continuum slope β (defined by $f_\lambda \propto \lambda^\beta$) provides information about the stellar populations and the interstellar medium (ISM) of the galaxies. Since the UV continuum is dominated by radiation from massive stars, β is sensitive to the metallicity and age of the stellar population, and especially the dust content within a galaxy (e.g. Cortese et al. 2008; Wilkins et al. 2011). At high redshifts $z \gtrsim 6$, because stellar populations are expected to be uniformly young (Tacchella et al. 2018b), β is believed to be mostly affected by dust extinction, making it a useful tracer of chemical enrichment and dust formation in early galaxies. Studies have found that galaxies are generally bluer with increasing redshift (Finkelstein et al. 2012; Bouwens et al. 2014), and that fainter galaxies are bluer than brighter ones (Bouwens et al. 2014). This implies that the dust content in galaxies is decreasing towards earlier times, and that faint galaxies may be less metal enriched than massive ones.

The sizes and morphologies of galaxies at $z \gtrsim 6$ offer another window into galaxy formation and evolution. Sizes are influenced by the host halo's angular momentum (e.g. Mo, Mao & White 1998), merger history, and also stellar feedback which can redistribute angular momentum within galaxies (Brooks et al. 2011; Genel et al. 2015; Christensen et al. 2016). The luminosity dependence of the galaxy sizes is also affected by the form of the dominating feedback (e.g. Wyithe & Loeb 2011). Observations have shown that galaxies at $z \gtrsim 6$ are very compact, with physical sizes of order 1 kpc or even smaller (e.g. Oesch et al. 2010). The bright galaxies are often found to contain multiple cores, which could be interpreted as merging systems or individual star-forming clumps within a larger structure or disc (e.g. Bowler et al. 2017). Observations of the galaxy size–luminosity relation have also put constraints on the specific angular momentum of the disc and the spin parameter of the halo (e.g. Shibuya, Ouchi & Harikane 2015; Kawamata et al. 2018), providing insights into the angular momentum transfer between discs and haloes.

Our theoretical picture of galaxy formation has been widely tested against the above-mentioned observations of galaxies at $z \gtrsim 6$, both by semi-analytic models (e.g. Yung et al. 2019a, b) and via cosmological simulations of galaxy formation (e.g. Davé, Finlator & Oppenheimer 2006; Finlator et al. 2006; Finlator, Davé & Oppenheimer 2007; Finlator, Oppenheimer & Davé 2011). To obtain the photometric properties of the model galaxies, different groups have used different recipes for dust extinction, combined with stellar population synthesis models. For instance, one can calculate the line-of-sight metal or dust column density (e.g. Khakhaleva-Li & Gnedin 2016; Cullen et al. 2017; Wilkins et al. 2017; Ma et al. 2018a; Vogelsberger et al. 2019; Katz et al. 2019), utilize full dust radiative transfer (e.g. Narayanan et al. 2018; Behrens et al. 2018; Ma et al. 2019; Vogelsberger et al. 2019), or perform full modelling of dust formation, evolution, and destruction, which

has been explored semi-analytically (e.g. Popping, Somerville & Galametz 2017; Vijayan et al. 2019), seminumerically (e.g. Mancini et al. 2015, 2016), and with numerical simulations (e.g. Bekki 2015a, b; McKinnon et al. 2017; Aoyama et al. 2017, 2018; Aoyama, Hirashita & Nagamine 2020). While it is desirable to include all details of dust modelling when comparing simulations to observations, the lack of observations at high redshifts also makes it difficult to test the predictions of the dust distribution in simulations. We thus aim to use simple assumptions about dust attenuation to examine the photometric properties of simulated high-z galaxies.

In this work, we study the photometric properties of galaxies at $z \approx 6$ from the SIMBA cosmological simulations (Davé et al. 2019), a successor to the MUFASA project (Davé, Thompson & Hopkins 2016). We examine the UVLF, UV continuum slope, and sizes of the simulated galaxies. SIMBA is calibrated to reproduce the global evolution of the galaxy mass function and quenched galaxy population from $z \sim 6 \rightarrow 0$, thus providing a plausible feedback model that can be tested against $z \gtrsim 6$ observations. In addition to investigating the nature of galaxies at the reionization -epoch, we make predictions for future *JWST* observations. *JWST* will allow us to probe the rest-frame optical radiation from those $z \sim 6$ galaxies, while *HST* cannot. It thus offers a window for understanding both the rest-UV and rest-optical observations and the link between them. We especially present our mock image generation routine, since the ability of cosmological simulations to resolve structures within galaxies provides a powerful tool to probe the morphologies of high-z galaxies (Ma et al. 2018b).

This paper is organized as follows. In Section 2, we briefly introduce the simulations and the tools we use to generate mock observations. Section 3 presents the UVLF, UV continuum slope, and size measurements from the simulated galaxies, and explores predictions for future *JWST* observation. We summarize our work in Section 4.

2 SIMULATIONS AND ANALYSIS

2.1 The SIMBA simulations

This work uses two new simulations in the SIMBA cosmological hydrodynamic simulation suite. We refer the readers to Davé et al. (2019) for a detailed description of the input physics, and summarize the main points here. SIMBA uses the GIZMO cosmological gravity + hydrodynamics code with its meshless finite mass solver (Hopkins 2015, 2017). It includes non-equilibrium radiative cooling from H, He, and metals, and incorporates star formation using an H_2-based Schmidt–Kennicutt relation (Kennicutt 1998). The H_2 fraction computed based on the subgrid prescription of Krumholz & Gnedin (2011), with a minimum metallicity of 1 per cent solar. Star formation-driven winds are modelled as kinetic decoupled two-phase outflows, with the mass loading factor scaling with stellar mass as given by Anglés-Alcázar et al. (2017b). Black holes are seeded and grown primarily using a torque-limited accretion model (Anglés-Alcázar et al. 2017a), and feedback is in the form of radiative winds, jets, and X-ray momentum. These modules work together to yield good agreement with a wide range of galaxy (Davé et al. 2019) and black hole (Thomas et al. 2019) observables across cosmic time.

We describe in more detail the metal enrichment, stellar feedback, and dust growth models below, which are the most relevant for our work. The chemical enrichment model tracks 11 elements (H, He, C, N, O, Ne, Mg, Si, S, Ca, and Fe) during the simulation,

with enrichment tracked from Type II SNe (Nomoto et al. 2006), Type Ia SNe (Iwamoto et al. 1999), and asymptotic giant branch (AGB) stars (Oppenheimer & Davé 2006). We note that SIMBA no longer applies an arbitrary reduction of yields by a factor of 2 that was previously needed to match the mass–metallicity relation (MZR), and instead lock individual metals into dust. The star formation-driven galactic winds are implemented as decoupled two-phase winds, with 30 per cent of wind particles ejected with a temperature set by the SN energy minus the wind kinetic energy. The mass loading factor η is a broken power law of stellar mass which follows results from the Feedback In Realistic Environments (FIRE) zoom simulations (Anglés-Alcázar et al. 2017b), but is capped constant below an M_* corresponding to 16 star particles. η is further suppressed at $z > 3$. These steps prevent excessive feedback so that poorly resolved galaxies can grow. The wind velocity scalings follow Muratov et al. (2015). SIMBA also implements metal-loaded winds, which extract some metals from nearby particles to represent the local enrichment by the SNe driving the wind.

Dust growth and destruction processes are tracked on the fly, where dust is passively advected following the gas particles. SIMBA assumes that dust grains have the same constant radius and density. Dust is produced by condensation of a fraction of metals from SNe and AGB ejecta, following the prescription by Popping et al. (2017). Once dust grains are seeded, they grow by accreting gas-phase metals, with an accretion time-scale following Hirashita (2000) and Asano et al. (2013). Dust grain erosion follows the approximation of the thermal sputtering rate of grain radii derived by Tsai & Mathews (1995). SIMBA implements a subgrid model for dust destruction by SN shocks (Dwek & Scalo 1980; Seab & Shull 1983; McKee et al. 1987; McKee 1989), and additionally destroy dust completely in hot winds and during star formation and AGN X-ray heating.

The simulation in Davé et al. (2019) had a $(100 \, h^{-1} \, \mathrm{Mpc})^3$ volume (SIMBA-100). Here, we run simulations with identical input physics but having volumes of $(25 \, h^{-1} \, \mathrm{Mpc})^3$ (denoted as SIMBA-25) and $(50 \, h^{-1} \, \mathrm{Mpc})^3$ (SIMBA-50). A minor modification to the SIMBA-100 mass loading factor scaling is that it is held constant at $M_* < 2.9 \times 10^8 \, \mathrm{M_\odot}$ (which is the SIMBA-100 galaxy mass resolution limit), rather than continuing its power law increase down to each simulation's galaxy mass resolution limit; this was found necessary in order to prevent very large mass loading factors in small early galaxies that oversuppressed early star formation. Like the large-volume SIMBA-100 run, these new runs also have 1024^3 dark matter particles and 1024^3 gas elements. As such they have mass resolutions $64 \times$ and $8 \times$ better than the SIMBA-100, respectively. This is necessary to better model small early galaxies. Specifically, SIMBA-25 has a dark matter particle mass resolution of $1.5 \times 10^6 \, \mathrm{M_\odot}$ and initial gas element mass resolution of $2.85 \times 10^5 \, \mathrm{M_\odot}$, with the corresponding numbers in SIMBA-50 being eight times larger. The minimum gravitational softening lengths are $0.125 \, h^{-1} \, \mathrm{kpc}$ (comoving) and $0.25 \, h^{-1} \, \mathrm{kpc}$ in SIMBA-25 and SIMBA-50, respectively. Notably, SIMBA-25 resolves haloes down to approximately the H cooling limit ($M_{\mathrm{halo}} \sim 10^8 \, \mathrm{M_\odot}$ at $z \sim 6$), so should capture the vast majority of cosmic star formation during the EoR. SIMBA-50 enables us to extend the dynamic range and test resolution convergence effects. SIMBA-25 and SIMBA-50 are run down to $z \approx 4$, but for this work we only use $z \geq 6$ snapshots. All runs adopt a Planck Collaboration XIII (2016) cosmology with $\Omega_m = 0.3$, $\Omega_\Lambda = 0.7$, $\Omega_b = 0.048$, $h = 0.68$, $\sigma_8 = 0.82$, and $n_s = 0.97$.

2.2 The galaxy sample

Galaxies are identified in post-processing using the YT-based package CAESAR, which uses a 6D friends of friends algorithm. We consider galaxies with ≥ 32 star particles. This gives us 13 622 galaxies in SIMBA-25, and 9588 in SIMBA-50 in the $z = 6$ snapshots. For the stellar mass function and the UVLF, we use all galaxies in this sample. For the UV continuum slope and size measurements, we only use galaxies with $M_{1500} \leq -16$ in SIMBA-25 and those with $M_{1500} \leq -18$ in SIMBA-50 when assuming the Calzetti et al. (2000) extinction law. These magnitude thresholds are the positions where the UVLFs turn over because the star formation histories cannot be adequately captured with the adopted mass resolutions (see Section 3 for details). This reduces our sample size to 2699 galaxies in SIMBA-25, and 2608 in SIMBA-50 at $z = 6$. We also briefly examine the stellar mass function and the UVLF at $z = 8$.

2.3 Mock photometry, images, and spectra

We use the PYLOSER package[1] to create synthetic spectra and images for the simulated galaxies. PYLOSER treats each star particle in a galaxy as a single stellar population with a given age and metallicity. It generates a mock spectrum for the star particle using the Flexible Stellar Population Synthesis (FSPS) library of population synthesis models (Conroy, Gunn & White 2009; Conroy & Gunn 2010). We include nebular emission, which is implemented in FSPS by a pre-computed CLOUDY table, implemented by Byler et al. (2017). By default, we use the MESA Isochrone Stellar Tracks (MIST, Dotter 2016; Choi et al. 2016; Paxton et al. 2011, 2013, 2015) and the Medium resolution INT Library of Empirical Spectra (MILES, Sánchez-Blázquez et al. 2006; Falcón-Barroso et al. 2011) and assume a Chabrier (2003) initial mass function (IMF). In Appendix A, we will show that using different isochrone models, especially one that includes stellar binaries, yields very similar UVLF and β–M_{1500} relation as using MIST. This is consistent with the findings of Choi, Conroy & Byler (2017) that the predictions on the far-UV spectrum by different isochrone models agree well with each other.

To take into account dust extinction, we first calculate the metal column density and the mass-weighted average metallicity along the line of sight to each star particle. The metal column density is converted to the total extinction in the *V* band, A_V, via the A_V–metal column density relation in the Milky Way (Watson 2011). We then scale the A_V value by the ratio of the dust-to-metal ratio (DTM) of the sightline to that of the Milky Way (Dwek 1998; Watson & Jakobsson 2012), where the DTM is calculated using the average metallicity of the sightline and a fitting formula to the simulated DTM–gas-phase metallicity relation of SIMBA-100 (Li, Narayanan & Davé 2019). We note that in principle we could compute the dust column density directly from the SIMBA outputs. We refrain from doing so because it is unclear how well the locally calibrated dust model works at $z \gtrsim 6$, owing to lack of observations and a lack of constraints on the input model parameters. There is also no straightforward way to convert the simulated dust distribution into amounts of extinction, without full dust radiative transfer. The A_V–metal column density relation is, in contrast, better constrained by observations. We therefore defer a more careful investigation of the dust model at these redshifts to future work, and continue with the approximation that dust traces metals.
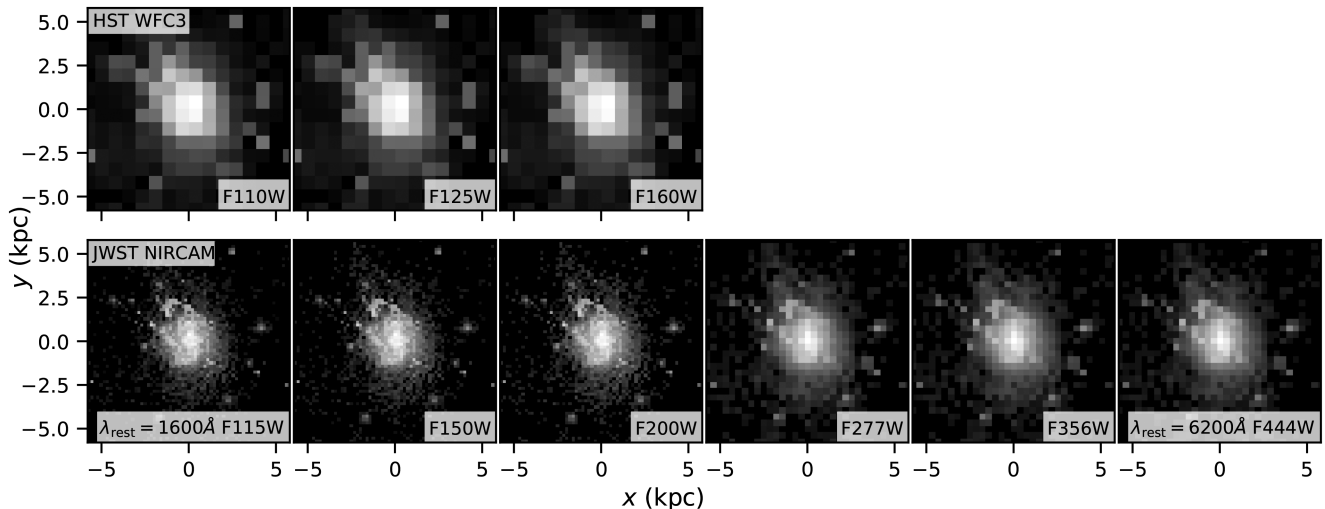
---

[1] https://pyloser.readthedocs.io/en/latest/

Figure 1. An example of the mock images of a galaxy in SIMBA-25 at $z = 6$ created with PYLOSER assuming the Calzetti et al. (2000) extinction law. This galaxy has a stellar mass of $6 \times 10^9\,M_\odot$, an SFR of $24\,M_\odot\,\text{yr}^{-1}$, a gas-phase SFR-weighted metallicity of $0.28\,Z_\odot$, and $M_{1500} = -20.88$. The x, y coordinates are in units of physical kpc. The images have a side length of four times the 3D stellar radius of the galaxy. Top and bottom panels show images in three *HST* IR bands and six *JWST* bands, created using the corresponding pixel scales. The wavelengths increase from left to right. The *JWST* F115W and F444W bands correspond to rest-frame 1600 and 6300 Å, respectively. The images are not convolved with PSFs and no noise has been added.

Given an A_V value for each star particle, we then extinct its spectrum by assuming an extinction law. We primarily use the Calzetti et al. (2000) law, but we also consider the extinction law from Salmon et al. (2016), which multiplies the Calzetti et al. (2000) law by $(\lambda/\lambda_V)^\delta$, where $\delta = 0.62\log E(B - V) + 0.26$ and $\lambda_V = 5500$ Å. Such a form lets galaxies with high colour excess have a shallower, starburst-like law, and those with low colour excess have a steeper, Small Magellanic Cloud (SMC)-like law. Finally, we also examine the SMC extinction law (Gordon et al. 2003). For creating the mock images, we only use the Calzetti et al. (2000) law since it yields the best match of the simulated UVLF and β–M_{1500} relation to observations (see below and Section 3).

For each CAESAR-identified galaxy, PYLOSER sums the spectra of all the star particles in it and convolves the summed spectra with desired filters to get the AB magnitudes. We use the rest-frame spectra to compute the absolute UV magnitudes, and the redshifted spectra to calculate the apparent magnitudes for relevant *HST* and *JWST* bands. The magnitude at rest-frame 1500 Å, M_{1500}, is calculated by the convolving the rest-frame spectra using a boxcar filter centred at 1500 Å with 400 Å in width. For the *JWST* bands, we especially focus on *JWST* F115W and F444W, which correspond to rest-frame 1600 and 6300 Å at $z = 6$. PYLOSER is also able to make mock images by binning the star particles into pixels, and analogously compute the magnitudes in each pixel. We use the pixel sizes of the corresponding *HST* and *JWST* bands to generate the images. Specifically, F115W and F444W have pixels scales of 0.031 and 0.063 arcsec, respectively, which correspond to 0.18 and 0.37 physical kpc at $z = 6$.

2.4 An example galaxy

To illustrate the sort of outputs obtainable from PYLOSER, we show images and spectra for a selected $z = 6$ galaxy from SIMBA-25. This galaxy has a stellar mass of $6 \times 10^9\,M_\odot$, a star formation rate (SFR) of $24\,M_\odot\,\text{yr}^{-1}$, and a gas-phase SFR-weighted metallicity of $0.28\,Z_\odot$.

Fig. 1 shows example images generated by PYLOSER for the selected galaxy in SIMBA-25 at $z = 6$ in various *HST* WFC3 and *JWST* Near-Infrared Camera (NIRCam) bands. The x, y coordinates are in units of physical kpc. The images are shown out to twice the 3D stellar radius of the galaxy, which is the largest distance of a star particle to the galaxy's centre of mass as determined by CAESAR. From left to right, the effective wavelengths of the filters increase. Each image is created using the corresponding pixel scale of the instrument/filter. The images are not convolved with point spread functions (PSFs) and no noise is added. In this optimal setup, *JWST* clearly resolves more detailed structures of the galaxy than *HST*, such as clumps, streams, and the central core. The *HST* WFC3 filters have a pixel scale of 0.13 arcsec, which is about four times and twice as large as the pixel scales of *JWST* F115W and F444W, respectively. Similarly, the *JWST* F115W image shows more structures than the F444W one. Interestingly, this galaxy has very similar morphologies in the rest-frame UV (e.g. F115W) and rest-frame optical (e.g. F444W) bands. In fact, we find that the simulated galaxies exhibit a general trend of having similar morphologies in rest-UV and rest-optical, owing to young ages of the stellar populations (see Section 3.4 for details).

Fig. 2 presents an example of mock spectra generated for the selected galaxy in SIMBA-25. The black line shows the extinction-free spectrum, and the blue, green, and red lines represent the attenuated spectrum assuming the Salmon et al. (2016), Calzetti et al. (2000), and SMC laws, respectively. Assuming the Calzetti et al. (2000) law, this galaxy has a UV magnitude of $M_{1500} = -20.88$ and $A_V = 0.88$.[2] Hence, this is a galaxy that is typically detectable with *HST* at these epochs. The Salmon et al. (2016) law exhibits the least extinction, while the SMC law generates the most dust attenuation. The galaxy displays a very blue continuum and strong emission lines characteristic of early galaxies, but also

---

[2] A_V is computed by subtracting the extincted galaxy spectrum from the extinction-free one, and convolving this with the Johnson V filter. Hence, it depends on the assumed extinction law. Different extinction laws results in $\lesssim 0.3$ differences in the A_V values.
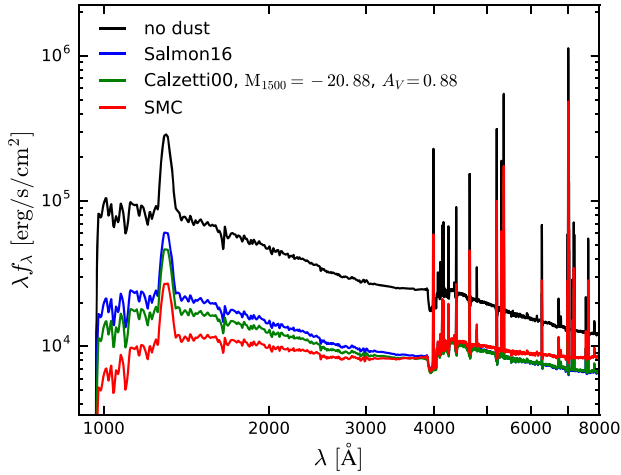
Figure 2. Mock spectra of the same galaxy as shown in Fig. 1 at $z = 6$, assuming no dust (black line), the Salmon et al. (2016) (blue), Calzetti et al. (2000) (green), and SMC (red) extinction laws. When using the Calzetti et al. (2000) extinction law, this galaxy has $M_{1500} = -20.88$ and $A_V = 0.88$.

shows a noticeable 4000 Å break indicating an underlying older stellar population.

3 MAIN RESULTS

3.1 The stellar mass function and the UVLF

Fig. 3 shows the stellar mass functions in SIMBA-25 (red lines) and SIMBA-50 (blue lines) at $z = 6$ (top panel) and $z = 8$ (bottom panel). Error bars represent a jackknife estimate of the error. Circles and triangles represent the observational data in Song et al. (2016) and Duncan et al. (2014), respectively.

The two simulations are in fairly good agreement with the observational data at both redshifts. Also, the good agreement between the two simulations in the overlapping mass range shows that they are reasonably well converged in mass growth. SIMBA-25 overshoots the number of low-mass galaxies at $z = 6$. While systematic uncertainties in the observations are generally larger here, this may indicate that SIMBA does not suppress very small galaxy formation sufficiently. We note that we suppressed the mass loading factor in low-mass galaxies at high redshift in order to achieve agreement in the SFR function of low-mass galaxies, and consequently in the UVLF that we will discuss in the next section, but this appears to still slightly overproduce the stellar mass in these galaxies.

Fig. 4 presents the simulated rest-frame 1500 Å LFs at $z = 6$ (top and middle panels) and $z = 8$ (bottom panel). Here, we use all galaxies in our sample, with no stellar mass limit, in order to assess resolution convergence. Since these small young objects are very gas-rich, they typically have $\gtrsim 100$ gas and star particles in total, which is generally regarded as sufficient to be well resolved. The red and blue lines in the top panel show the $z = 6$ UVLFs in SIMBA-25 and SIMBA-50, respectively. Solid and dashed lines represent UVLFs assuming no dust and the Calzetti et al. (2000) extinction law, respectively. Error bars illustrating the jackknife estimate of the error are only plotted for the dust-attenuated UVLFs.

The UVLFs in the two simulations are reasonably well converged in the M_{1500} range where they overlap. The SIMBA-25 UVLF shows a turnover at $M_{1500} = -16$, and SIMBA-50 at $M_{1500} = -18$. These
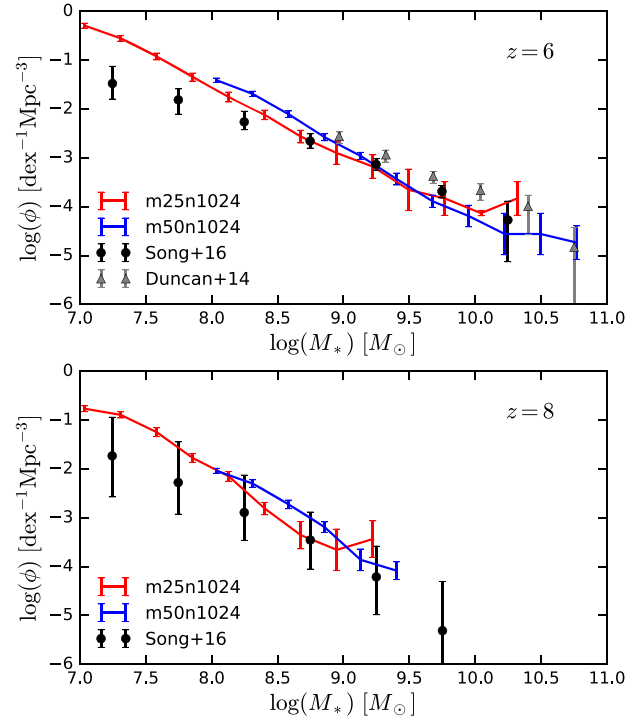
Figure 3. The galaxy stellar mass functions at $z = 6$ (top panel) and $z = 8$ (bottom panel). Red and blue lines represent the mass functions in SIMBA-25 and SIMBA-50, respectively. Error bars show a jackknife estimate of the error. Circles and triangles illustrate the observational data in Song et al. (2016) and Duncan et al. (2014), respectively. The two simulations roughly match the observational data at both redshifts.

turnovers are not physical. They occur because the mass resolutions of these simulations can no longer adequately capture the star formation histories of the low-mass galaxies, owing to our stochastic approach to star formation which occurs quite rarely in such small systems with high mass loading factors. Therefore in the analysis on the UV continuum slope and size measurements below, we only focus on galaxies with $M_{1500} \leq -16$ in SIMBA-25, and those with $M_{1500} \leq -18$ in SIMBA-50.

We combine UVLFs in SIMBA-25 and SIMBA-50 by taking the value of the combined LF in each M_{1500} bin to be the higher one of the LFs in the two simulations (following Davé et al. 2006).[3] The middle panel of Fig. 4 illustrates the combined UVLFs from SIMBA-25 and SIMBA-50 at $z = 6$. The green dashed, dotted–dashed, solid, and dotted lines represent the combined UVLFs assuming no dust, the Salmon et al. (2016) law, Calzetti et al. (2000) law, and the SMC law, respectively. The observational data shown by black circles is a compilation of the data in Bouwens et al. (2015, 2017) and Finkelstein et al. (2015).

The no-dust UVLF clearly overshoots the number of bright galaxies, showing that despite the UVLF being at face value

---

[3]We note that our approach of combining the LFs tends to bias the combined LF high. One might prefer an weighted average, but there is no obvious way to determine the weights, since one needs to define which simulation is 'better' and meanwhile take into account cosmic variance. Taking the maximum value of each bin is well defined, since the small box simulation is incomplete at the bright end and the large box is incomplete at the faint end. We have also verified that taking a number-squared weighted average of the LFs (e.g. Vogelsberger et al. 2019) yields very similar results as taking the maximum value.
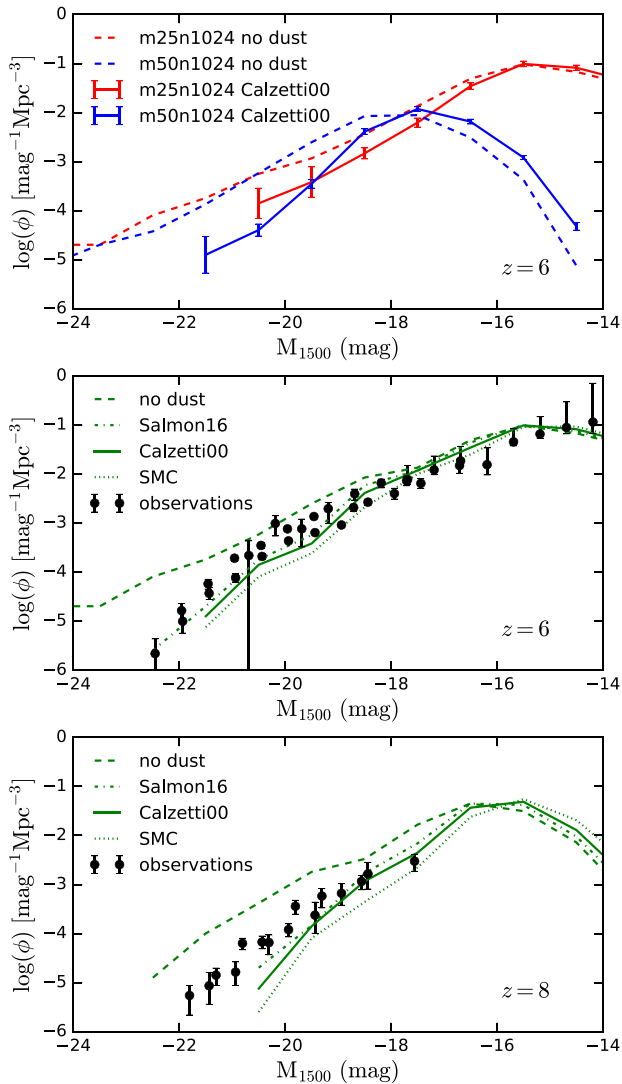
Figure 4. Top: the $z = 6$ UVLFs in *SIMBA*-25 (red) and *SIMBA*-50 (blue). Solid lines represent UVLFs using the Calzetti et al. (2000) extinction law, and dashed lines show the no dust LFs. Error bars represent a jackknife estimate of the error and are only plotted for the dust-attenuated UVLFs. Middle: combined $z = 6$ LFs of *SIMBA*-25 and *SIMBA*-50. Green dashed, solid, dotted–dashed, and dotted lines show LFs assuming no dust, Calzetti et al. (2000) law, Salmon et al. (2016) law, and SMC law, respectively. Black circles represent the observational data compiled from Bouwens et al. (2015), Finkelstein et al. (2015), and Bouwens et al. (2017). Bottom: similar to the middle panel, but showing results at $z = 8$. Observational data come from Bouwens et al. (2015) and Finkelstein et al. (2015). The UVLF is not very sensitive to the dust extinction law. The simulations roughly match the observations at $z = 6$, but underpredict the number of bright galaxies at $z = 8$ with dust attenuation.

consistent with a power law, in fact the brightest UV galaxies at these epochs must already be substantially dust-attenuated. All three extinction laws yield simulated UVLFs that are in agreement with the observations. The SMC law produces the most dust attenuation, so the bright end of the LF is suppressed a bit more. Similarly, the Salmon et al. (2016) law gives more bright galaxies, but the differences produced by the three extinction laws are too small to be distinguishable with the observational data. This indicates that current measures of the UVLF are not strongly sensitive to the dust attenuation law assumed, for reasonable choices. An agreement

Table 1. Faint-end slopes of the simulated UVLFs at $z = 6$ (top row) and 8 (bottom row), fitted using galaxies with $-19 < M_{1500} < -16$. Middle and right-hand columns list the slopes without dust and with the Calzetti et al. (2000) extinction law, respectively.

Redshift	Slope without dust	Slope with Calzetti law
6	-1.6	-1.7
8	-1.7	-1.9

between the simulated dust-attenuated UVLF and the observations has also been found in a number of previous works using different assumptions on dust properties and post-processing techniques (e.g. Khakhaleva-Li & Gnedin 2016; Mancini et al. 2016; Wilkins et al. 2017; Ma et al. 2018a, 2019). While the effect of dust attenuation is already observable at $M_{1500} < -18$ in *SIMBA*, other works seem to show that dust extinction starts becoming important for $M_{1500} < -20$ at such high redshift. This indicates that the *SIMBA* galaxies have a bit more dust extinction at $z = 6$. As we will show below, this effect is more prominent at $z = 8$.

The bottom panel of Fig. 4 is similar to the middle panel, but showing results at $z = 8$. Interestingly, the no-dust UVLF still overshoots the observations of Bouwens et al. (2015) and Finkelstein et al. (2015), but all the dust-attenuated UVLFs now underpredict the number of galaxies with $M_{1500} < -18$. One possibility is that the assumed normal stellar populations and IMF used to generate the UV emission is reasonable at $z \sim 6$, but at $z \sim 8$ they under-predict the UV flux. Another possibility is that there is too much dust attenuation in the simulations at these epochs. The latter seems more likely given the large difference between the no-dust and dust-attenuated UVLFs at $z = 8$ compared to $z = 6$. We will examine the physical reason for this excess dust extinction in Section 3.3.

Overall, the *SIMBA* stellar mass function and UVLF are in descent agreement with observations at $z = 6$ and 8, albeit the $z = 8$ UVLF being a bit low. Before moving on to the UV continuum slope, we briefly comment on the faint-end slope of the UVLF. Table 1 lists the faint-end slopes of the simulated UVLFs at $z = 6$ (top row) and 8 (bottom row), fitted using galaxies with $-19 < M_{1500} < -16$. Middle and right-hand columns list the slopes without dust and with the Calzetti et al. (2000) extinction law, respectively. Generally, we find values shallower than -2, which may be slightly inconsistent with observations (e.g. Bouwens et al. 2015, 2017; Finkelstein et al. 2015). However, we have not attempted to estimate uncertainties in simulations, which come from both resolution effects and subgrid models. Caution therefore needs to be taken when interpreting the faint-end slopes of the simulated UVLF.

3.2 The UV continuum slope

A more stringent test of dust attenuation is provided by examining the UV continuum slope β. We compute β by fitting a power-law slope using the three rest-frame magnitudes at rest-frame 1500, 2300, and 2800 Å, which roughly mimics the observational procedure. We have verified that fitting a power law to the rest-frame spectra directly yields very similar results.

Fig. 5 shows the simulated β–M_{1500} relations at $z = 6$. Colours and linestyles are the same as in Fig. 4. The top panel compares the results from *SIMBA*-25 (red) and *SIMBA*-50 (blue), without dust attenuation (dashed) and assuming Calzetti et al. (2000) law (solid). Error bars represent 1σ spread in β within the galaxy sample. As motivated in Section 3.1, we only use galaxies with $M_{1500} \leq$
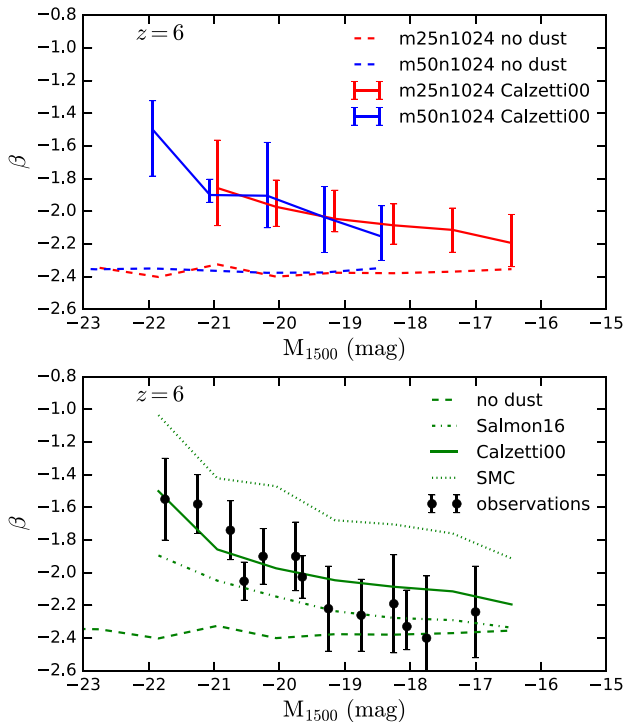
Figure 5. Top: the $z = 6$ UV continuum slope (β)–UV luminosity (M_{1500}) relations in SIMBA-25 (red) and SIMBA-50 (blue). Solid and dashed lines represent the β–M_{1500} relations assuming the Calzetti et al. (2000) extinction law and no dust, respectively. Error bars illustrate 1σ spread in β and are only shown for the dust-attenuated β–M_{1500} relations. Bottom: combined β–M_{1500} relations of SIMBA-25 and SIMBA-50. The green dashed, solid, dotted–dashed, and dotted lines represent the relations assuming no dust, Calzetti et al. (2000), Salmon et al. (2016), and SMC laws respectively. Black circles showing the observational data are compiled from Bouwens et al. (2014) and Finkelstein et al. (2012). The β–M_{1500} relation is sensitive to the dust-attenuation law, and the Calzetti et al. (2000) law gives the best fit to the observations.

-16 in SIMBA-25 and those with $M_{1500} \leq -18$ in SIMBA-50. The two simulations are well converged in the M_{1500} range where they overlap.

Without dust attenuation, the β–M_{1500} relations are flat, indicating that all galaxies have similar ages and metallicities. This is because the SFR–stellar mass relation in the simulations at $z \approx 6$–8 has a slope of ≈ 1. Thus all galaxies require similar amounts of time to assemble their stellar masses, leading to roughly constant age with stellar mass (see also Tacchella et al. 2018b). This flat no-dust β is consistent with the findings of Khakhaleva-Li & Gnedin (2016) and Mancini et al. (2016). Other simulations, for example Mancini et al. (2016), Wilkins et al. (2017), and Ma et al. (2018a), also found either a flat sSFR or a flat mass-weighted age across different stellar masses, confirming our explanation. Hence the trend in the simulated β mostly arises from the differences in dust attenuation in the galaxies. In reality, β is also a function of the uncertain metallicity of stellar population and the star formation history. Changes in these two quantities can lead to a change in β by up to <0.3 (Wilkins et al. 2011; Tacchella et al. 2018a). This is much smaller than a change in β induced by a change in A_V or the dust extinction law, which we find to be at $\Delta\beta \sim 0.8$ level (see analysis below). Therefore β is most sensitive to the dust attenuation and can be a good tracer of the dust extinction law.
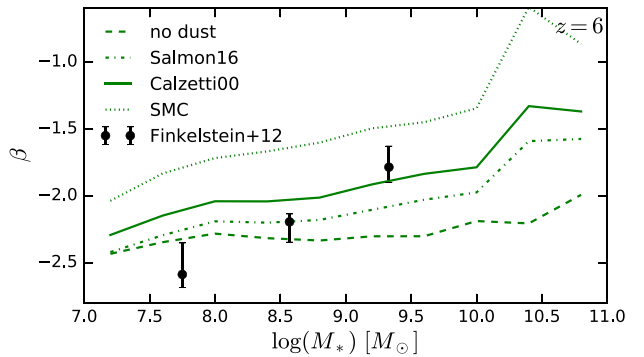
Figure 6. Combined β–M_* relations of SIMBA-25 and SIMBA-50 at $z = 6$. The green dashed, solid, dotted–dashed, and dotted lines represent the relations assuming no dust, Calzetti et al. (2000), Salmon et al. (2016), and SMC laws respectively. Black circles show the observational data from Finkelstein et al. (2012). The observations indicate much steeper changes of β with stellar mass.

The bottom panel of Fig. 5 combines the samples from SIMBA-25 and SIMBA-50 to show β–M_{1500}, illustrating the effects of our three different extinction laws: Salmon et al. (2016, dotted–dashed), Calzetti et al. (2000, solid), SMC (dotted), and no dust (dashed). We compare to observational data of Bouwens et al. (2014) and Finkelstein et al. (2012) shown as the black circles. Overall, SIMBA predicts more dust attenuation in brighter galaxies. This broadly agrees with Ma et al. (2019) who showed that a heavy attenuation is required to reproduce the observed bright-end UVLFs at $z \geq 5$.

The SMC law, which reddens the galaxy spectra the most (see Fig. 2), produces the shallowest UV continuum slopes and thus a β–M_{1500} relation that is too high ($\Delta\beta \sim 0.4$) compared to the observations. In contrast, the Salmon et al. (2016) law has the least extinction and hence generates bluer galaxies with the lowest β–M_{1500} relation. It roughly matches the observational data at $M_{1500} > -20$, but makes the bright galaxies slightly too blue compared to the observations ($\Delta\beta \sim -0.3$). The Calzetti et al. (2000) law yields the overall best match of the simulations to the observations, though it would be even slightly better if faint galaxies had a flatter attenuation law like that of Salmon et al. (2016). The best-fitting law being Calzetti et al. (2000) may be in some tension with observations such as Salmon et al. (2016) and Reddy et al. (2016) which tend to show less far-UV attenuation than Calzetti et al. (2000). We note that there is some degeneracy between β and the intrinsic far-UV emission slope, which may be impacted by different stellar populations such as more binaries or Population III stars. Given such uncertainties, the broad agreement of SIMBA with observations assuming a Calzetti et al. (2000) attenuation law is preliminarily encouraging. Our finding that the simulations favour the Calzetti et al. (2000) law against the SMC law is also consistent with the simulation work of Cullen et al. (2017), though Mancini et al. (2016) found that an SMC-like extinction law with a clumpy dust distribution is preferred. A full exploration of the dust extinction law at $z \sim 6$ thus requires dust radiative transfer, which we will defer to future work.

Finally, we examine the dependence of β on stellar mass, since Finkelstein et al. (2012) found a more significant correlation of β with M_*, than with M_{1500}. Fig. 6 shows the simulated β–M_* relations at $z = 6$, combined from SIMBA-25 and SIMBA-50. Linestyles are the same as in the bottom panel of Fig. 5. Since M_{1500} and M_* are tightly correlated, the overall trend of the simulated β–M_* relation is expected not to change much from that of β–M_{1500}. However, the

observations of Finkelstein et al. (2012) clearly show a steeper β–M_* relation than our simulations. Khakhaleva-Li & Gnedin (2016) also found a tighter correlation between β and M_* in their simulations, but we note that the correlation only gets steep for $M_* < 10^7\,M_\odot$, so our findings roughly agree with theirs. This indicates a possible tension between observations and simulations. One issue could be an observational selection effect that the lowest mass galaxies are more visible if they are younger and less dust-attenuated, which may bias towards lower β values. Future *JWST* observations will be able to lower the uncertainties in determining both β and M_*, thus providing stronger constraints on the correlation.

In summary, SIMBA produces a β–M_{1500} relation in good agreement at $z = 6$, assuming the Calzetti et al. (2000) extinction law. We also examined this at $z = 8$, but the dynamic range is small and the uncertainties are large owing to the small number of galaxies in both observations and SIMBA, so this was not particularly enlightening. IR spectroscopy with *JWST* to more directly constrain the typical extinction curve in $z \gtrsim 6$ systems will prove quite valuable at discriminating between models of early galaxy and dust growth, and thus potentially provide indirect constraints on mass outflow rates.

3.3 The metal enrichment of reionization-epoch galaxies

We now examine the origin of the dust-attenuated $z = 8$ UVLF being low compared to observations, as found in Section 3.1. Since we apply an attenuation based on the line-of-sight gas-phase metal column density to each star and modify the A_V values using the simulated DTM–gas-phase metallicity relation, our finding hints upon possible early metal enrichment in the simulations that leads to too high A_V values. Fig. 7 examines the gas-phase MZR (top panel) and the DTM–metallicity scaling (bottom panel) in SIMBA at $z = 6$ (green) and $z = 8$ (magenta). SIMBA-25 and SIMBA-50 galaxies have been combined to produce the overall relation; they agree well in the overlap region. The shaded regions illustrate 1σ spread in metallicity and DTM. The solid lines represent the median metallicity and linear fits to the DTM–Z relations in the top and bottom panels, respectively. There are no observations yet of the MZR at $z = 6$–8, but for comparison we show observations at $z \approx 2$ from the MOSFIRE Deep Evolution Field (MOSDEF) survey (Sanders et al. 2015) and those at $z = 3$–4 by Troncoso et al. (2014) and Onodera et al. (2016). We note that SIMBA-100 well reproduces the MZR at $z \sim 2$ (Davé et al. 2019), and we would expect SIMBA-25 and SIMBA-50 to do so as well if they were run down to that redshift.

The MZR predicted in SIMBA-25 and SIMBA-50 is consistent with the $z = 3$–4 observations, although the observations have large scatter and the inferred metallicity depends strongly on the assumed strong-line calibration. Remarkably, the simulated MZR is higher at $z \sim 6$–8 than at $z = 2$. This may seem counterintuitive at first, because metallicity is often regarded as a cumulative record of past star formation. However, as Finlator & Davé (2008), Davé, Finlator & Oppenheimer (2012), and others have argued, in fact this is not correct when the inflow rates are large. Instead, the MZR reflects a recent balance between inflows and outflows, approximately given by $Z \approx y\dot{M}_{in}/(1 + \eta)$, where y is the yield, $\dot{M}_{in}$ is the accretion rate on to the ISM, and η is the mass loading factor. The mass dependence and evolution of the MZR thus reflects that of the inflow rate and mass loading factor.

In SIMBA, we attenuate the high-z mass loading factor in small galaxies ($M_* < 2.9 \times 10^8\,M_\odot$) by forcing a constant mass loading factor below this mass. This was found to be necessary to generate
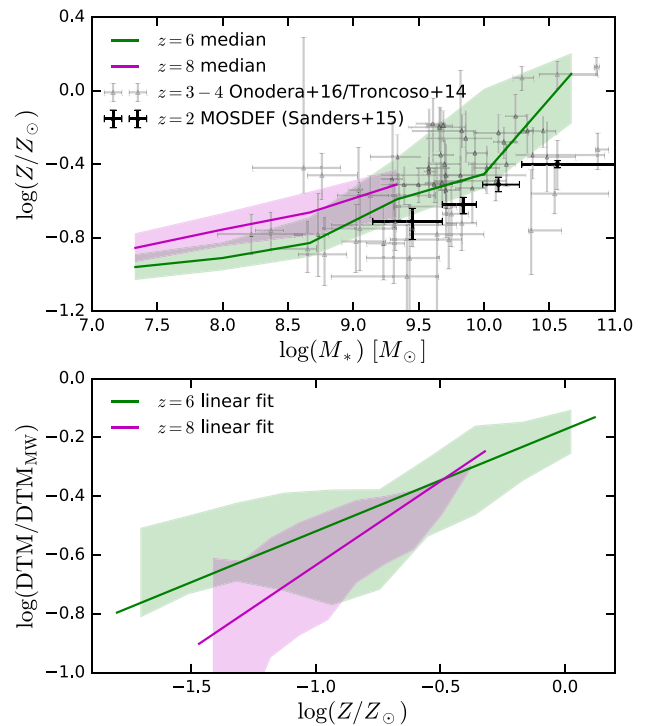

Figure 7. Top: gas-phase MZRs in SIMBA-25 and SIMBA-50 at $z = 6$ (green) and $z = 8$ (magenta). Solid lines show the median gas-phase MZRs, and shaded regions represent 1σ spread in the metallicity. Black dots with error bars show the observational data from the MOSDEF survey at $z = 2$ (Sanders et al. 2015), and grey triangles represent the $z = 3$–4 observations of Onodera et al. (2016) and Troncoso et al. (2014). Bottom: simulated DTM–gas-phase metallicity relations at $z = 8$ and 6. Shaded regions show 1σ spread in DTM, and solid lines represent power-law fits which are used to calculate the UVLF with PYLOSER. SIMBA predicts early metal enrichment and high metallicities that would lead to too much dust extinction, which is partly mitigated by a steep DTM that reduces the A_V values of faint galaxies.

early galaxy growth as observed; if we extrapolated our mass-dependent η to very small systems, we end up with extremely large values of η that prevent any early growth at all. With this choice, we are able to broadly reproduce observed early stellar mass growth.

However, this choice also means that the MZR has a different mass and redshift dependence than at lower redshifts. First off, because η at low masses is independent of M_*, this results in a flatter $Z(M_*)$ up to our chosen cut-off M_*. Also, because mass accretion rates are generally higher at high redshifts, and this is not mitigated by high η values, this means that the predicted MZR is actually higher at high redshifts (see also the analysis in Langan, Ceverino & Finlator 2019; Torrey et al. 2019).

Returning to the UVLF, one effect of the higher MZR is lower UV flux output owing to stellar populations with correspondingly higher metallicity, especially in the range 0.1–$1.0\,Z_\odot$. We have verified that the stellar metallicities in the simulated galaxies roughly trace the gas-phase metallicities, with ~ 0.2 dex scatter. Changing the stellar metallicity from 0.1 to $1.0\,Z_\odot$ at $z = 6$–8 lowers the galaxy UV luminosity by ~ 0.4 mag (see fig. 3 of Tacchella et al. 2018b). However, the simulated no-dust UVLF surpasses the observations. The reduced UV flux is therefore not the main reason for the simulated $z = 8$ UVLF being low.

We thus examine in detail the second effect of a higher MZR on the UVLF, which is an increase in the amount of dust extinction. Since the $z = 6$–8 MZR in SIMBA is higher than the observations at

$z = 2$, simply applying the A_V–metal column density scaling of the Milky Way (see Section 2) would result in too much dust extinction. However, the steep DTM–Z scaling as shown in the bottom panel of Fig. 7 lowers the A_V values of the faint galaxies, leading to descent agreement between the simulated $z = 6$ UVLF and the observations. At $z = 8$, the DTM of most galaxies are lower than at $z = 6$, but the even higher metallicities seem to be too extreme, resulting in too much dust extinction that lowers the UVLF. This suggests that our assumption of η at $z \gg 6$ in very small galaxies may need some modification. Doing so may also help alleviate the discrepancy in the faint-end mass function of SIMBA-25. We leave it for future work to tune this more carefully. We note that while our assumed $\eta(M_*)$ is taken from that predicted in the FIRE simulations (Anglés-Alcázar et al. 2017b), FIRE does not offer strong guidance for this quantity at these very early epochs.

Focusing on $z \sim 6$, the fact that the high MZR predicted by SIMBA is able to match the observed UVLF and β–M_{1500} relation indicates the possibility of early metal enrichment. Whether such early metal enrichment is necessary to reproduce the $z \sim 6$ observations is slightly sensitive to the DTM ratio. If the subgrid model locks significantly more metals into dust, the MZR would be lower and we may still be able to reproduce the UVLF. However, any significant reduction in the MZR would require very large DTM ratios that are not predicted by SIMBA (Li et al. 2019), nor expected owing to the time taken to grow dust grains from metals. Future *JWST* observations will be able to constrain the metal enrichment history of these reionization-epoch galaxies with near-IR spectroscopy.

3.4 Galaxy size and morphology

A unique new capability of *JWST* will be to able to resolve typical reionization-epoch galaxies in the rest-frame optical, as is evident from Fig. 1. With *HST*, this is only possible in the rest-frame UV, and for fairly sizeable galaxies unless they are lensed. It is thus interesting to make predictions for *JWST* to understand the relationship between rest-UV and rest-optical sizes. We do so here by making mock images with PYLOSER and mimicking the observational procedure to determine galaxy sizes. Along the way we will also compare to available *HST* observations of $z \approx 6$ galaxy sizes.

We focus on sizes in the *JWST* F115W and F444W bands, which correspond to rest-frame 1600 Å (UV) and 6300 Å (optical) at $z = 6$, respectively.[4] The former is similar to the *HST* F110W band, and we obtain very similar sizes in these two bands when extracted at the same resolution. For each simulated galaxy, we generate mock *JWST* images in these two bands with a side length of four times the maximum radius of the star particles to the galaxy's centre of mass. Given that the Calzetti et al. (2000) extinction law produces the overall best match of the simulations to the observed UVLF and β–M_{1500} relation at $z = 6$, we only use the Calzetti et al. (2000) law to generate mock images. We perform size measurements using three methods listed below:

(i) *Growth curve method:* we generate both the F115W images and the F444W images using the F115W pixel scale, 0.031 arcsec. F444W images created in this way are denoted as high resolution (F444W-HR). We compute the flux weighted centre of the images and perform circular aperture photometry with the PYTHON `photutils`[5] package to get the growth curve. This is used to measure the half-light radius which contains half of the total light of the galaxy.

(ii) *Sérsic fit method:* we produce the F115W and F444W images using their original pixel scales, 0.031 and 0.063 arcsec, respectively.[6] The images are then convolved with the PSFs of the two bands.[7] We add Gaussian noise with a standard deviation that corresponds to 1/50 of the median flux of the image. This choice of the noise level is arbitrary, but does not affect our size measurement much because a larger effect comes from the PSF. We then use `photutils` to produce a segmentation map, which is an integer-valued 2D array where pixels belonging to the same source are labelled with the same integer value. The background is tagged as zero in the segmentation map. We only keep the source with the largest area and smooth the main source segment by convolving the segmentation map with a uniform boxcar filter spanning 4 pixels in each dimension. This segmentation map and the PSF are fed into the STATMORPH package[8] to fit a Sérsic (1968) profile to the galaxy image and obtain the half-light radius r_e (Rodriguez-Gomez et al. 2019). The Sérsic profile parametrizes the surface brightness profile of a galaxy as

$$\Sigma(r) = \Sigma_0 \exp\left[-b_n \left(\frac{r}{r_e}\right)^{1/n}\right] \tag{1}$$

where Σ_0 is the surface brightness at $r = r_e$, b_n is a coefficient chosen so that a circular aperture with radius r_e contains half of the galaxy's flux, and n is the Sérsic index. STATMORPH also takes a segmentation map and the PSF as input. During each step of the Sérsic profile fitting, the modelled Sérsic profile is convolved with the PSF to correct for the PSF effects. We keep all galaxies whose 'bad measurement' flags are 0, indicating good measurements (`flag` and `flag_sersic`; see Rodriguez-Gomez et al. 2019, for details). This is a much looser selection criterion than that used in Rodriguez-Gomez et al. (2019) because we would like to keep more data. The 'good fit' criteria depend on other input parameters as well, such as the gain (which we set to 1). We therefore avoid removing a large fraction of galaxies out of our sample so as not to bias our results. However, we caution that r_e values that fall below the PSF FWHM (full width at half-maximum) of the filters are unlikely to be reliable.

(iii) *3D half-light method:* we calculate the fluxes in F115W and F444W for each star particle in a galaxy and compute a light-weighted centre. We then measure the 3D half-light radius for the galaxy, which can be seen as the 'intrinsic' size of the galaxy. The dust extinction of each star particle is calculated along the same line of sight as the one adopted when producing the mock images. While

---

[4]We choose to focus on F115W simply because it is close to rest-frame 1500 Å at $z = 6$. We note that JWST/NIRCam is undersampled in F115W, so F150W or F200W may be a better choice for size measurements. However, the undersampling problem can be mitigated by drizzling. Moreover, given the similarity of galaxy morphologies in F115W and F444W as presented in Section 3.4, we anticipate that using F150W or F220W instead of F115W will not affect our main conclusions.

[5]https://photutils.readthedocs.io

[6]We note that in real observations people usually combine a few tens of exposures, thereby drizzle them on to a smaller grid. Thus, in reality the drizzled pixel scales can be smaller by a factor of about 2 than the original pixel scales (0.031 and 0.063 arcsec) used in this work.

[7]Downloaded from https://jwst-docs.stsci.edu/near-infrared-camera/nircam-predicted-performance/nircam-point-spread-functions; generated by WEBBPSF (Perrin et al. 2012; Perrin et al. 2014).

[8]https://statmorph.readthedocs.io

in this case a 2D half-light radius seems better defined, in practice we find that the differences between the 2D and 3D sizes are only at ~ 20 per cent level. Therefore, our analysis are not significantly affected by the choice of definition of the sizes.

Fig. 8 illustrates the steps of the Sérsic fit method. Top and bottom panels show images in F115W and F444W, respectively. The images are shown out to twice the 3D stellar radius of the galaxy, which is the largest distance of a star particle to the galaxy's centre of mass as determined by CAESAR. The leftmost column shows the original images of the same galaxy in SIMBA-25 as shown in Fig. 1. The second column presents the images after being convolved with PSFs in the two bands and added Gaussian noise. The best-fitting Sérsic profile models convolved with PSFs are shown in the third column. Finally, the rightmost column shows the normalized residual of the Sérsic fit. The 'bad measurement' flags of this galaxy all indicate successful Sérsic fits, but not all the features can be fully fitted. This is not surprising given that early small galaxies are often fairly irregular and clumpy in SIMBA, as is also the case in observations. None the less, the Sérsic fit captures much of the overall profile.

3.4.1 Size–luminosity relation

Fig. 9 shows the (rest-UV) size–luminosity relations at $z = 6$ obtained using the growth curve method, the Sérsic fit method, and the 3D half-light method from left to right. The sizes are measured in the F115W band and shown in units of physical kpc, and plotted versus M_{1500}. Red and blue lines illustrate results in SIMBA-25 and SIMBA-50, respectively. Error bars represent the 1σ spread in the sizes. In the left-hand and middle panels, the green and orange dashed lines show the F115W pixel scale and the PSF FWHM, respectively. The black lines show the observed size–luminosity relation in Kawamata et al. (2018), and the shaded region represent 1σ error. Kawamata et al. (2018) measured the sizes of a sample of galaxies obtained in the Hubble Frontier Fields program by correcting the lensing effects and fitting Sérsic profiles to the stacked images in the WFC3/IR bands.

The simulated size–luminosity relations are reasonably converged between the two simulations, using all three methods. Given that the nominal resolution of SIMBA-50 is about 50 physical pc at this redshift, and half that in SIMBA-25, and the F115W pixel scale is ~ 4 times larger than this, it is not surprising that the predictions are robust to resolution effects, at least down the sizes probed by *JWST*.

The galaxy sizes measured using the two observational approaches (growth curve and Sersic) agree well with *HST* observations. The brightest galaxies have sizes of about a physical kpc, whereas galaxies at $M_{1500} \approx -17$ to -18 approach the instrumental resolution; below this, it will be difficult to robustly measure sizes without the aid of lensing. Sizes measured with growth curve method that fall below the F115W pixel scale (green dashed line) are not fully trustable. Similarly, sizes obtained with the Sérsic method should be trusted when they are larger than the PSF FWHM (orange dashed line). The 3D half-light radii agree with the two observational methods for the bright galaxies. The sizes of faint galaxies show a steeper decline than the observational data, indicating potential systematic errors in observations below the instrumental resolution limits.

We examine how well the measured sizes using the three different methods recover the true 3D half-stellar mass radii. Fig. 10 illustrates the ratio of the F115W (rest-UV) sizes to the 3D half-stellar mass radii as a function of stellar mass, with the F115W sizes obtained by the three methods. We have combined sampled from SIMBA-25 and SIMBA-50. Solid green lines represent the median of the ratios, and the shaded regions show 1σ spread in the size ratios. For the growth curve method and 3D half-light radii, we also show results using the no-dust sizes with magenta lines.

Focusing first on the right-hand panel of Fig. 10, the no-dust 3D half-light sizes are $20 - 50$ per cent smaller than the 3D half-stellar mass radii, but the ratios are roughly constant. This indicates that although more concentrated than mass, light traces mass well in these simulated $z = 6$ galaxies, so these galaxies can only have weak age gradients. When including dust extinction, the sizes could be a factor of 1.5–3 larger than sizes without dust for galaxies with $M_* \gtrsim 10^9 \, \mathrm{M_\odot}$, and also overestimate the half-mass radii by up to a factor of ~ 1.5. This suggests that the centres of the galaxies are more dust-attenuated. Indeed, we will show in Section 3.4.3 that the centres of these galaxies are younger but with more dust extinction. Results obtained with the two observational methods are generally similar, as shown in the left-hand and middle panels. The sizes of galaxies with $M_* < 10^8 \, \mathrm{M_\odot}$ are overestimated by factors of 1.5–2, owing to the finite resolution of the mock images and smoothing of the PSF.

Overall, SIMBA produces galaxy sizes that are in good agreement with current *HST* observations at $z = 6$. We also find that the observed sizes are a biased tracer of the true half-stellar mass radii. Moving forward, we will explore predictions for *JWST* observations.

3.4.2 Rest-optical versus rest-UV sizes

Since future *JWST* observations will be able to explore the $z \sim 6$ galaxies in the rest-frame optical wavelengths, we explore how the rest-frame optical sizes compare with the rest-frame UV ones. Fig. 11 shows comparisons between the F444W (rest-optical) sizes and the F115W (rest-UV) sizes, measured using the growth curve method, the Sérsic fit method, and 3D half-light method from left to right, respectively. The green dashed line in the leftmost panel indicate the F115W pixel scale. The orange and yellow dashed lines in the middle panel represent the PSF FWHM of F115W and F444W, respectively. In the rightmost panel showing the intrinsic 3D half-light radii, the F115W and F444W sizes match each other very well. This is surprising because for galaxies at much lower redshifts where the cores are redder and the discs are bluer, the rest-frame optical sizes should be smaller than the rest-frame UV sizes (e.g. Szomoru et al. 2013; Lang et al. 2014; Tacchella et al. 2015a, b; Mosleh et al. 2017). Our size measurements at $z = 6$ therefore indicates young stellar populations and small age gradients with radius in these high-z galaxies. We note that although the sizes presented here include effects of dust extinction, the no-dust sizes also show a good one-to-one relation between rest-UV and rest-optical.

The sizes measured with the two observational approaches make very similar predictions as the theoretical method on the sizes in rest-frame UV and optical. The growth curve method is limited by the finite pixel size, but still produces a clear one-to-one trend (shown by the black diagonal line) of the sizes in the two bands. Our finding slightly disagrees with Ma et al. (2018b), who also measured sizes with mock images but found that the FIRE-2 $z = 6$ galaxies have very clumpy UV morphologies and that the rest-optical traces the stellar mass better than UV. However, their galaxies are fainter ($M_{1500} > -18$) than ours. Moreover, the FIRE-2 galaxies have been shown to have bursty star formation histories owing to their star formation feedback model (Muratov et al. 2015; Sparre et al.
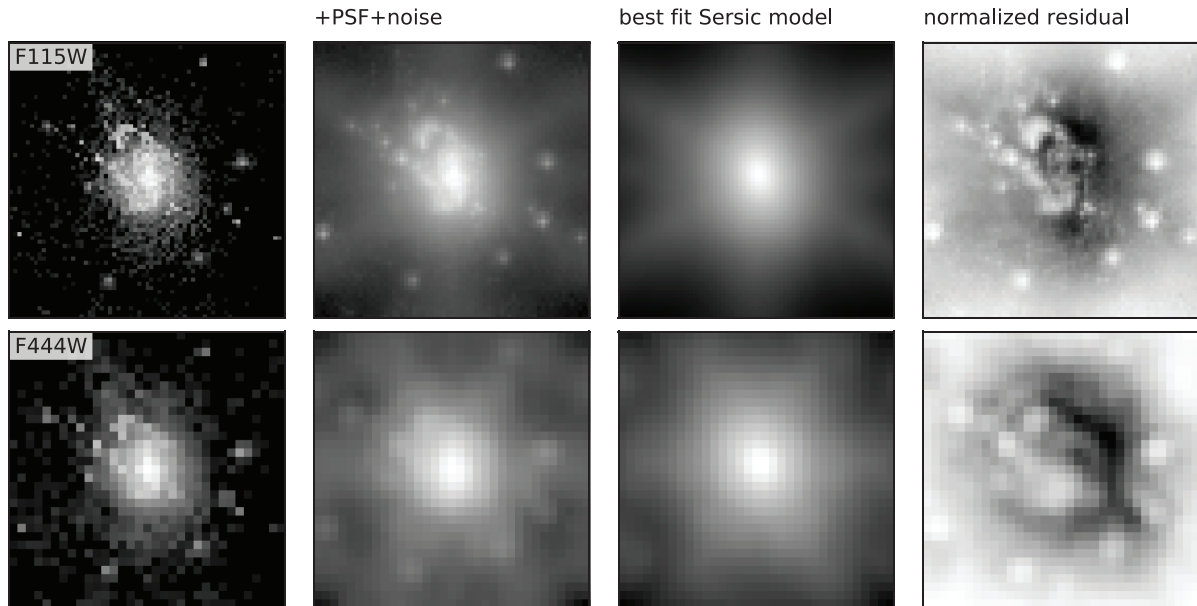
Figure 8. An illustration of our image generation and Sérsic fit pipeline. Top and bottom panels show mock *JWST* F115W and F444W images, respectively. The leftmost column presents the original images of a galaxy in SIMBA-25. The images are centred at the centre of mass of the galaxy, and have a side length of four times the 3D stellar radius of the galaxy. The second column shows images convolved with PSFs in the corresponding bands and added Gaussian noise with a standard deviation corresponding to 1/50 of the median flux of the image. The third column illustrates the Sérsic fit results, with the PSFs convolved. The normalized residual of the Sérsic fit are shown in the rightmost column.
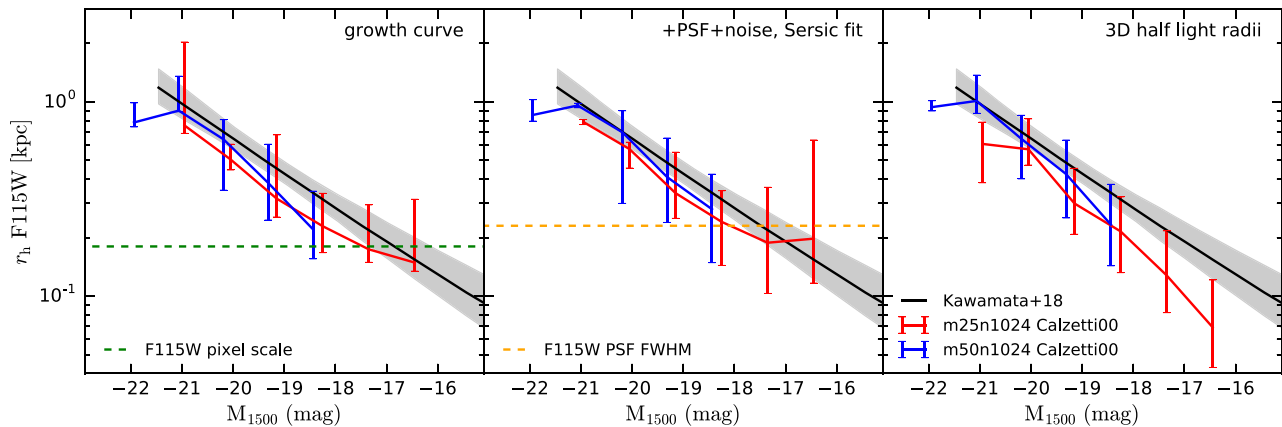
Figure 9. The size–UV luminosity relations measured in the *JWST* F115W band (rest-frame UV) at $z = 6$. From left to right, sizes are obtained using the growth curve method, the Sérsic fit method, and the 3D half-light method, respectively (see the text for details). Red and blue represent results obtained from SIMBA-25 and SIMBA-50, respectively. Error bars show 1σ spread in the sizes. For the growth curve and Sérsic fit methods, we generate images assuming the Calzetti et al. (2000) law. For the 3D half-light method, the size measurements shown use the dust-attenuated flux in F115W. All methods yield a descent match to the observed size–luminosity relation.

2017; Ma et al. 2018a), making them more likely to have clumpy morphologies than the SIMBA galaxies. The Sérsic fit method gives more scatter in the measured sizes, primarily owing to the smoothing by the PSFs. The similarity in the F115W and F444W sizes can still be seen. However, because of the large FWHM of the F444W PSF (0.83 physical kpc at $z = 6$) compared to the physical sizes of the galaxies (of order ~ 1 kpc), a lot of the Sérsic fit results go below the FWHM of the F444W PSF (horizontal dashed yellow line). The $z \sim 6$ galaxies thus still require lensing in order for their size measurements in the rest-frame optical bands to be reliable with the observations of *JWST*.

3.4.3 Color, dust, and age gradients

We now explore the age and A_V gradients in the simulated galaxies in detail. Fig. 12 presents maps of the *JWST* F115W − F444W (rest-UV − rest-optical) colour, A_V, and age, created for two galaxies in SIMBA. The maps have the same pixel size as F115W, 0.031 arcsec. The galaxy shown in the top row has $M_* = 2.3 \times 10^9 \, \mathrm{M_\odot}$ and SFR= $7.4 \, \mathrm{M_\odot \, yr^{-1}}$, and the one in the bottom row has $M_* = 4.9 \times 10^9 \, \mathrm{M_\odot}$ and SFR= $40 \, \mathrm{M_\odot \, yr^{-1}}$. The maps are shown out to twice the 3D stellar radius of the galaxy, which is the largest distance of a star particle to the galaxy's centre of mass as determined by CAESAR.
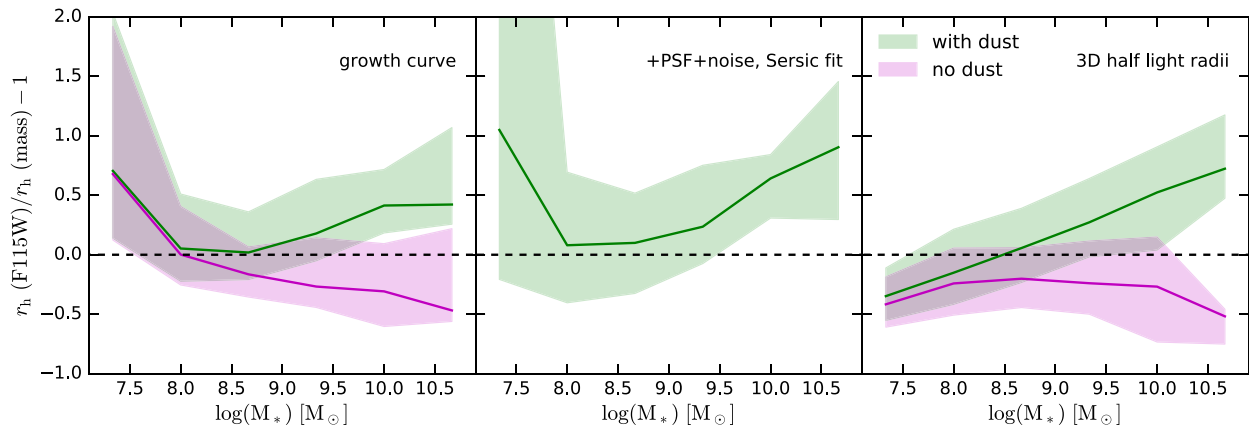
Figure 10. Similar to Fig. 9, but showing comparisons of the measured F115W sizes (rest-UV) to the galaxy 3D half-stellar mass radii as a function of stellar mass. Shaded regions represent 1σ spread in the size ratios. The 3D half-light radii traces the half-mass radii very well at $z = 6$. Due to the finite pixel size and smoothing by the PSF, size measurements in real observations bias the 'true' sizes, which we find to be a mass-dependent effect.
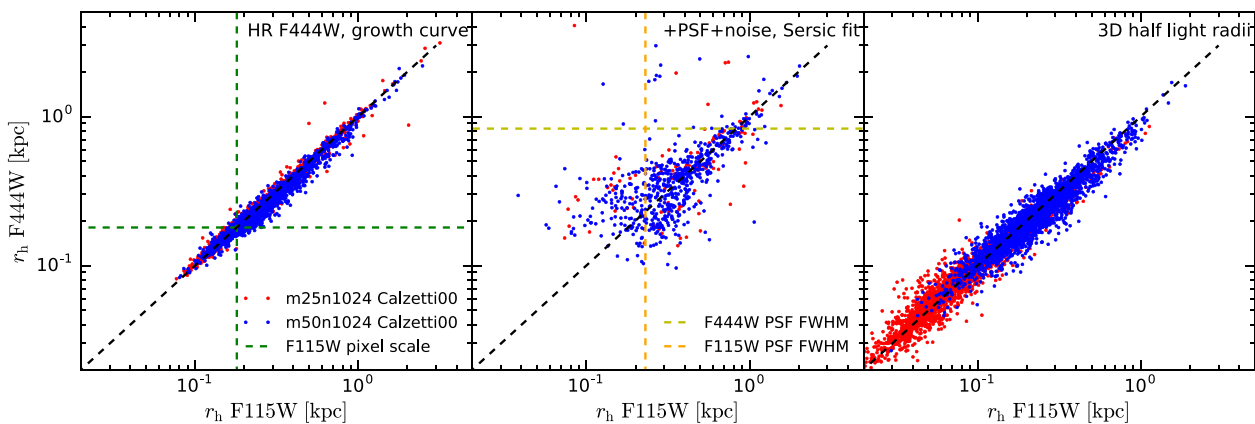

Figure 11. Similar to Fig. 9, but showing comparisons between F444W (rest-optical) sizes and F115W (rest-UV) sizes at $z = 6$. The green dashed lines in the left-hand panel show the pixel scale of *JWST* F115W. The orange and yellow dashed lines in the middle panel represent the FWHM of the PSFs in F115W and F444W, respectively. We did not remove galaxies with F444W sizes smaller than the PSF FWHM, but we caution that such size measurements may not be reliable. Regardless of the size measurement method used, the F115W (rest-UV) and F444W (rest-optical) sizes are very similar.

With dust extinction, the galaxies exhibit roughly uniform F115W − F444W colour (leftmost column), with the top galaxy having a slightly redder core and the bottom one having a slightly bluer core. Without dust, the core is clearly bluer in the centre (second column), especially for the bottom galaxy. Both galaxies have A_V maps that peak in the centre (third column), as expected since this is where the densest gas resides, and also the metallicity is higher in the core. The effect is stronger for the bottom galaxy. Also stronger for the bottom galaxy is the age gradient (rightmost column), with a very young core compared to the top one, which is perhaps related to the fact that the bottom galaxy has a three times higher specific SFR (sSFR). Interestingly, the galaxy in the bottom row shows an off-centre star-forming clump near the lower left corner which also has high A_V values, suggesting that giant clumps as seen in $z \sim 2$ galaxies may also be evident at these epochs. Curiously, the combined impact of the younger core with higher A_V seems to approximately cancel out in the F115W − F444W colour, leaving a mildly bluer core in the bottom galaxy. In the top galaxy, there is essentially no young core, and a weak A_V gradient, leading to a slightly redder core.

These results indicate that the weak age gradients of the simulated $z = 6$ galaxies make the centres of the galaxies bluer,

while more dust in the central star-forming regions makes them redder. The two effects weaken the colour gradients of the galaxies, leading to very similar rest-UV and rest-optical sizes. This finding also explains the differences among the sizes with dust, without dust, and the stellar half-mass radii. Breaking this well-known age–dust degeneracy would ideally require longer wavelength data with *JWST* Mid-Infrared Instrument (MIRI), although such data will be more limited in sensitivity and resolution as compared with NIRCam data. These maps demonstrate how reionization-epoch galaxies may be different from those at lower redshifts, which might be testable with future *JWST* observations.

Finally, we briefly comment on how the adopted DTM affects the sizes and morphologies of the simulated galaxies. Since the DTM increases with metallicity in SIMBA (Fig. 7), the higher metallicity regions, i.e. the star-forming central parts of the galaxies, are more dust-attenuated than what would be expected assuming constant DTM. Therefore if we measured the sizes using constant DTM, the differences between the sizes with and without dust would be lower (Fig. 10). However, given the age gradients in the simulated galaxies are small, we expect that the rest-UV and rest-optical sizes
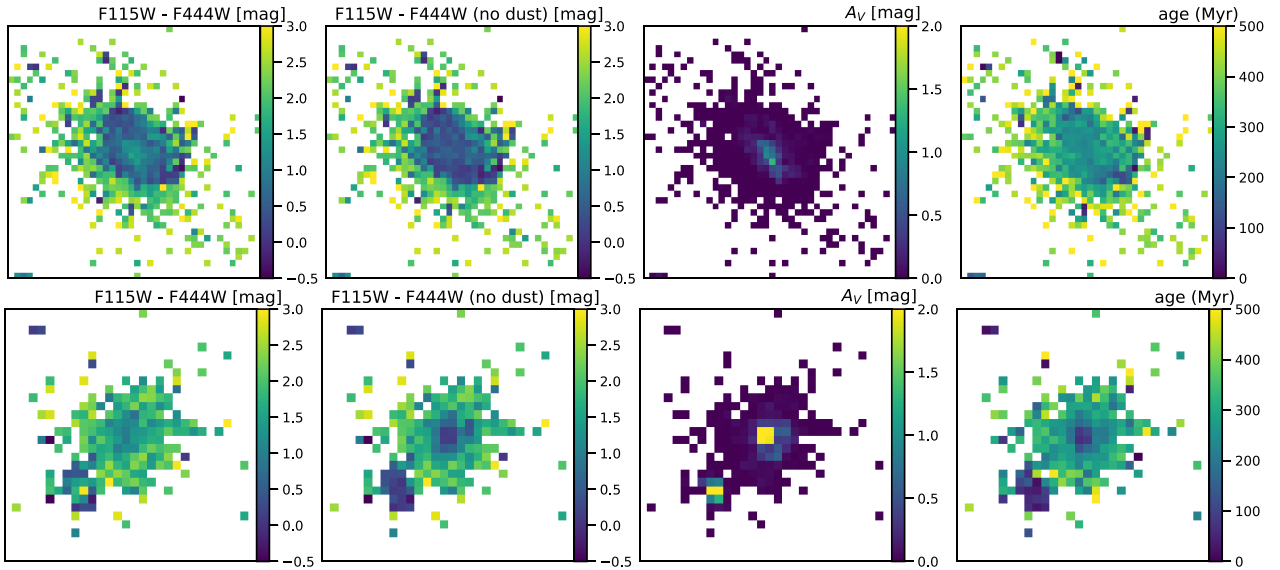
Figure 12. Examples of maps of *JWST* F115W − F444W colours with (leftmost column) and without dust (second column), A_V (third column), and age (rightmost column), created with two $z = 6$ galaxies in SIMBA. These maps do not include PSF effects. The galaxy shown in the top row has $M_* = 2.3 \times 10^9 \, \mathrm{M_\odot}$ and SFR= 7.4 $\mathrm{M_\odot \, yr^{-1}}$, and the one in the bottom row has $M_* = 4.9 \times 10^9 \, \mathrm{M_\odot}$ and SFR= 40 $\mathrm{M_\odot \, yr^{-1}}$. The maps have the same pixel scale as F115W, 0.031 arcsec (0.18 proper kpc at $z = 6$). These maps indicate weak age gradient which makes the centre of the galaxies bluer, while more dust in the centre makes it redder and thus weakens the colour gradient of the galaxies.

would still be very similar if assuming constant DTM (Fig. 11). We note that we have implicitly assumed that dust tracks metals, and that in principle one would prefer using dust radiative transfer to fully take into account of the dust distribution. Moreover, several authors (e.g. Khakhaleva-Li & Gnedin 2016; Ma et al. 2019) have pointed out the importance of correctly modelling dust scattering when comparing simulations to observations. These aspects will be explored in detail in future work.

In summary, SIMBA produces very similar rest-optical and rest-UV sizes at $z = 6$, and thus predicts that early galaxies do not exhibit the more concentrated mass distribution relative to UV light as observed at lower redshifts. Future *JWST* observations may be able to test our prediction of the central dust-obscured star formation and weak age gradients in the $z = 6$ galaxies, which differ from the findings of galaxies at lower redshifts.

4 SUMMARY

In this work, we study the photometric properties of reionization-epoch galaxies in the cosmological hydrodynamic simulations from the SIMBA suite having $25 \, h^{-1} \, \mathrm{Mpc}$ (SIMBA-25) and $50 \, h^{-1} \, \mathrm{Mpc}$ (SIMBA-25) volumes. SIMBA-25 reaches resolutions $\lesssim 50$ pc physical at $z = 6$ and resolves all hydrogen cooling haloes, and SIMBA-50 exhibits good resolution convergence in all properties while allowing larger objects to be represented. Our main results are highlighted below:

(i) SIMBA produces reasonable agreement with the observed $z = 6$ UVLF, owing to a partial cancellation between the relatively high metallicities in the simulated galaxies and a steep DTM–gas-phase metallicity relation. We find that the UVLF at $M_{1500} \gtrsim -21$ is not sensitive to the form of the dust extinction law assumed. SIMBA underproduces the UVLF at $z = 8$, which may be caused by too few massive galaxies but more likely because of too much metal that increases the amount of dust extinction.

(ii) When assuming a Calzetti et al. (2000) extinction law, SIMBA produces a relationship between the UV continuum slope β and

M_{1500} in very good agreement with available observations at $z = 6$, with a hint that the shallower Salmon et al. (2016) modification is preferred for faint galaxies. We find that β is a good tracer of the dust extinction law, with the Salmon et al. (2016) law and the SMC law producing $\Delta\beta \sim 0.8$. Without dust, the simulated β–M_{1500} relation is flat, owing to the simulated SFR–stellar mass relations at $z = 6$–8 having a slope of ≈ 1. This results in similar amounts of time to double the stellar masses in different galaxies, thus similar ages and metallicities of the stellar populations.

(iii) The gas-phase metallicities of SIMBA galaxies at a given M_* are higher at $z = 6$ than at $z = 2$. At $z = 8$, SIMBA predicts an even higher MZR. The higher metallicity affects both the UV flux output of stellar populations and the amount of dust attenuation, but more significantly the latter. This metallicity evolution is understandable within a simple scenario where the gas-phase metallicity reflects a balance of pristine inflow versus enriched outflow, given the assumed mass outflow rates in SIMBA. A more fine-tuning of the mass loading factor in low-mass galaxies may mitigate the tension between the low-mass end of simulated stellar mass function and the observations at $z = 6$, as well as the simulated UVLF and the observations at $z = 8$. Nevertheless, the fact that the simulated $z = 6$ UVLF and β–M_{1500} relation match the observations hints upon the possibility of early enrichment in high-redshift galaxies, which will be testable with future *JWST* observations.

(iv) We measured the sizes of the simulated $z = 6$ galaxies by generating mock *JWST* images in the F115W (rest-UV) and F444W (rest-optical) bands. We find that SIMBA produces F115W size–M_{1500} relations that are in reasonable agreement with the observations of *HST*, regardless of whether the size measurement mimics the methods used in real observations, or is performed by theoretical calculations.

(v) We find that the simulated galaxies have very similar sizes in rest-UV and rest-optical, regardless of the method of size measurement. This has great implications for *JWST* because it will be able to observe the $z = 6$ galaxies in the rest-optical bands. Most simulated galaxies have sizes below the FWHM of the F444W PSF,

indicating that lensing is needed for their size measurements to be trustable.

(vi) We find that without dust extinction, light traces mass well in the simulated galaxies, owing to weak age gradients and young stellar populations. With dust extinction, the galaxy sizes can be factors of 1.5–3 larger than the stellar half-mass radii for $M_* \gtrsim 10^9 \, M_\odot$, since the highly star-forming regions are also the most dust-extincted. The observed sizes can thus be a biased tracer of the half-mass radii.

(vii) We find that the simulated galaxies show younger ages and more dust-obscured star formation in the inner parts, with age gradients accompanying similar extinction gradients. These two effects approximately counteract each other to produce weak F115W − F444W colour gradients in the simulated $z = 6$ galaxies, leading to very similar rest-UV and rest-optical sizes. This prediction is very different from the findings of the colour gradients of galaxies at lower redshifts, and thus will be interesting to test with future *JWST* observations.

Future observational facilities including *JWST* will be able to yield more accurate measurements of $z \gtrsim 6$ galaxies, such as the stellar population properties and the enrichment histories. Accompanying multiwavelength observations such as with the Atacama Large Millimeter/submillimeter Array (ALMA) will be crucial for providing an independent measure into the gas content and SFR, thereby giving independent avenues for constraining physical properties if such measures can be robustly interpreted within galaxy formation models (e.g. Leung et al. 2020). Galaxy formation simulations such as SIMBA thus can provide promising directions for future observations to probe, which in turn will act as direct tests of the input physical models. It is of particular interest to compare the predictions from simulations with different galaxy formation models. For instance, the Illustris-TNG50 simulation has a comparable volume and resolution as SIMBA, and allows for a statistical examination of the galaxy population properties (Nelson et al. 2019; Pillepich et al. 2019). Such simulations can also provide a rich data base for a thorough mimicking of the observational methods in order to understand the bias between the observed quantities and the underlying physical properties. It would also be interesting to perform full dust radiative transfer to test the robustness of the predictions presented in this work, which would make full use of the dust model in SIMBA and take into account important physical effects not considered here, such as dust scattering.

REFERENCES

Anglés-Alcázar D., Davé R., Faucher-Giguère C.-A., Özel F., Hopkins P. F., 2017, MNRAS, 464, 2840

Anglés-Alcázar D., Faucher-Giguère C.-A., Kereš D., Hopkins P. F., Quataert E., 2017, MNRAS, 470, 4698

Aoyama S., Hirashita H., Nagamine K., 2020, MNRAS, 491, 3844

Aoyama S., Hou K.-C., Hirashita H., Nagamine K., Shimizu I., 2018, MNRAS, 478, 4905

Aoyama S., Hou K.-C., Shimizu I., Hirashita H., Todoroki K., Choi J.-H., Nagamine K., 2017, MNRAS, 466, 105

Asano R. S., Takeuchi T. T., Hirashita H., Inoue A. K., 2013, Earth Planets Space, 65, 213

Atek H., Richard J., Kneib J.-P., Schaerer D., 2018, MNRAS, 479, 5184

Behrens C., Pallottini A., Ferrara A., Gallerani S., Vallini L., 2018, MNRAS, 477, 552

Bekki K., 2015, ApJ, 799, 166

Bekki K., 2015, MNRAS, 449, 1625

Bouwens R. J., Oesch P. A., Illingworth G. D., Ellis R. S., Stefanon M., 2017, ApJ, 843, 129

Bouwens R. J. et al., 2014, ApJ, 793, 115

Bouwens R. J. et al., 2015, ApJ, 803, 34

Bowler R. A. A., Dunlop J. S., McLure R. J., McLeod D. J., 2017, MNRAS, 466, 3612

Brooks A. M. et al., 2011, ApJ, 728, 51

Byler N., Dalcanton J. J., Conroy C., Johnson B. D., 2017, ApJ, 840, 44

Calzetti D., Armus L., Bohlin R. C., Kinney A. L., Koornneef J., Storchi-Bergmann Th., 2000, ApJ, 533, 682

Chabrier G., 2003, PASP, 115, 763

Choi J., Conroy C., Byler N., 2017, ApJ, 838, 159

Choi J., Dotter A., Conroy C., Cantiello M., Paxton B., Johnson B. D., 2016, ApJ, 823, 102

Christensen C. R. et al., 2016, ApJ, 824, 57

Conroy C., Gunn J. E., 2010, ApJ, 712, 833

Conroy C., Gunn J. E., White M., 2009, ApJ, 699, 486

Cortese L., Boselli A., Franzetti P., Decarli R., Gavazzi G., Boissier S., Buat V., 2008, MNRAS, 386, 1157

Cullen F., McLure R. J., Khochfar S., Dunlop J. S., Dalla Vecchia C., 2017, MNRAS, 470, 3006

Davé R., Anglés-Alcázar D., Narayanan D., Li Q., Rafieferantsoa M. H., Appleby S., 2019, MNRAS, 486, 2827

Davé R., Finlator K., Oppenheimer B. D., 2006, MNRAS, 370, 273

Davé R., Finlator K., Oppenheimer B. D., 2012, MNRAS, 421, 98

Davé R., Thompson R., Hopkins P. F., 2016, MNRAS, 462, 3265

Dotter A., 2016, ApJS, 222, 8

Duncan K. et al., 2014, MNRAS, 444, 2960

Dwek E., 1998, ApJ, 501, 643

Dwek E., Scalo J. M., 1980, ApJ, 239, 193

Eldridge J. J., Stanway E. R., Xiao L., McClelland L. A. S., Taylor G., Ng M., Greis S. M. L., Bray J. C., 2017, PASA, 34, e058

Falcón-Barroso J. et al., 2011, A&A, 532, A95

Finkelstein S. L. et al., 2012, ApJ, 756, 164

Finkelstein S. L. et al., 2015, ApJ, 810, 71

Finkelstein S. L. et al., 2019, ApJ, 879, 36,

Finlator K., Davé R., 2008, MNRAS, 385, 2181

Finlator K., Davé R., Oppenheimer B. D., 2007, MNRAS, 376, 1861

Finlator K., Davé R., Papovich C., Hernquist L., 2006, ApJ, 639, 672

Finlator K., Oppenheimer B. D., Davé R., 2011, MNRAS, 410, 1703

Genel S., Fall S. M., Hernquist L., Vogelsberger M., Snyder G. F., Rodriguez-Gomez V., Sijacki D., Springel V., 2015, ApJ, 804, L40

Gordon K. D., Clayton G. C., Misselt K. A., Landolt A. U., Wolff M. J., 2003, ApJ, 594, 279

Hirashita H., 2000, PASJ, 52, 585

Hopkins P. F., 2015, MNRAS, 450, 53

Hopkins P. F., 2017, preprint (arXiv:1712.01294)

Iwamoto K., Brachwitz F., Nomoto K., Kishimoto N., Umeda H., Raphael Hix W., Thielemann F.-K., 1999, ApJS, 125, 439

Katz H., Laporte N., Ellis R. S., Devriendt J., Slyz A., 2019, MNRAS, 484, 4054

Kawamata R., Ishigaki M., Shimasaku K., Oguri M., Ouchi M., Tanigawa S., 2018, ApJ, 855, 4
Kennicutt R. C., 1998, ApJ, 498, 541
Khakhaleva-Li Z., Gnedin N. Y., 2016, ApJ, 820, 133
Krumholz M. R., Gnedin N. Y., 2011, ApJ, 729, 36
Langan I., Ceverino D., Finlator K., 2019, MNRAS, 494, 1988
Lang P. et al., 2014, ApJ, 788, 11
Leung T. K. D., 2020, preprint (arXiv:2004.11912)
Li Q., Narayanan D., Davé R., 2019, MNRAS, 490, 1425
Livermore R. C., Finkelstein S. L., Lotz J. M., 2017, ApJ, 835, 113
Mancini M., Schneider R., Graziani L., Valiante R., Dayal P., Maio U., Ciardi B., 2016, MNRAS, 462, 3130
Mancini M., Schneider R., Graziani L., Valiante R., Dayal P., Maio U., Ciardi B., Hunt L. K., 2015, MNRAS, 451, L70
Mason C. A., Trenti M., Treu T., 2015, ApJ, 813, 21
Ma X. et al., 2018, MNRAS, 477, 219
Ma X. et al., 2018, MNRAS, 478, 1694
Ma X. et al., 2019, MNRAS, 487, 1844
McKee C., 1989, in Allamandola L. J., Tielens A. G. G. M., IAU Symp. 135, Interstellar Dust, Kluwer Academic Publishers, Dordrecht, p. 431
McKee C. F., Hollenbach D. J., Seab G. C., Tielens A. G. G. M., 1987, ApJ, 318, 674
McKinnon R., Torrey P., Vogelsberger M., Hayward C. C., Marinacci F., 2017, MNRAS, 468, 1505
Mo H. J., Mao S., White S. D. M., 1998, MNRAS, 295, 319
Mosleh M., Tacchella S., Renzini A., Carollo C. M., Molaeinezhad A., Onodera M., Khosroshahi H. G., Lilly S., 2017, ApJ, 837, 2
Muratov A. L., Kereš D., Faucher-Giguère C.-A., Hopkins P. F., Quataert E., Murray N., 2015, MNRAS, 454, 2691
Naidu R. P., Tacchella S., Mason C. A., Bose S., Oesch P. A., Conroy C., 2019, ApJ, 892, 109,
Narayanan D., Davé R., Johnson B. D., Thompson R., Conroy C., Geach J., 2018, MNRAS, 474, 1718
Nelson D. et al., 2019, MNRAS, 490, 3234
Nomoto K., Tominaga N., Umeda H., Kobayashi C., Maeda K., 2006, Nucl. Phys. A, 777, 424
Oesch P. A. et al., 2010, ApJ, 709, L21
Onodera M. et al., 2016, ApJ, 822, 42
Oppenheimer B. D., Davé R., 2006, MNRAS, 373, 1265
Paxton B., Bildsten L., Dotter A., Herwig F., Lesaffre P., Timmes F., 2011, ApJS, 192, 3
Paxton B. et al., 2013, ApJS, 208, 4
Paxton B. et al., 2015, ApJS, 220, 15
Perrin M.D., Sivaramakrishnan A., Lajoie C.-P., Elliott E., Pueyo L., Ravindranath S., Albert L., 2014, Proc. SPIE, 9143, 91433X
Perrin M.D., Soummer R., Elliott E.M., Lallo M.D., Sivaramakrishnan A., 2012, Proc. SPIE, 8442, 84423D
Pillepich A. et al., 2019, MNRAS, 490, 3196
Planck Collaboration et al., 2016, A&A, 594, A13
Popping G., Somerville R. S., Galametz M., 2017, MNRAS, 471, 3152
Reddy N. A., Steidel C. C., Pettini M., Bogosavljević M., 2016, ApJ, 828, 107
Robertson B. E. et al., 2013, ApJ, 768, 71
Rodriguez-Gomez V. et al., 2019, MNRAS, 483, 4140
Salmon B. et al., 2016, ApJ, 827, 20
Salpeter E. E., 1955, ApJ, 121, 161
Sanders R. L. et al., 2015, ApJ, 799, 138
Schechter P., 1976, ApJ, 203, 297
Seab C. G., Shull J. M., 1983, ApJ, 275, 652
Shibuya T., Ouchi M., Harikane Y., 2015, ApJS, 219, 15
Somerville R. S., Davé R., 2015, ARA&A, 53, 51
Song M. et al., 2016, ApJ, 825, 5
Sparre M., Hayward C. C., Feldmann R., Faucher-Giguère C.-A., Muratov A. L., Kereš D., Hopkins P. F., 2017, MNRAS, 466, 88
Stanway E. R., Eldridge J. J., 2018, MNRAS, 479, 75
Stark D. P., 2016, ARA&A, 54, 761
Szomoru D., Franx M., van Dokkum P. G., Trenti M., Illingworth G. D., Labbé I., Oesch P., 2013, ApJ, 763, 73
Sánchez-Blázquez P. et al., 2006, MNRAS, 371, 703

Sérsic J. L., 1968, Atlas de Galaxias Australes, Obs. Astron., Univ. Nac. Córdoba, Córdoba
Tacchella S., Bose S., Conroy C., Eisenstein D. J., Johnson B. D., 2018b, ApJ, 868, 92
Tacchella S., Trenti M., Carollo C. M., 2013, ApJ, 768, L37
Tacchella S. et al., 2015a, ApJ, 802, 101
Tacchella S. et al., 2015b, Science, 348, 314
Tacchella S. et al., 2018a, ApJ, 859, 56
Thomas N., Davé R., Anglés-Alcázar D., Jarvis M., 2019, MNRAS, 487, 5764
Torrey P. et al., 2019, MNRAS, 484, 5587
Troncoso P. et al., 2014, A&A, 563, A58
Tsai J. C., Mathews W. G., 1995, ApJ, 448, 84
Vijayan A. P., Clay S. J., Thomas P. A., Yates R. M., Wilkins S. M., Henriques B. M., 2019, MNRAS, 489, 4072
Vogelsberger M. et al., 2019, MNRAS, 492, 5167
Watson D., 2011, A&A, 533, A16
Watson D., Jakobsson P., 2012, ApJ, 754, 89
Wilkins S. M., Bunker A. J., Stanway E., Lorenzoni S., Caruana J., 2011, MNRAS, 417, 717
Wilkins S. M., Feng Y., Di Matteo T., Croft R., Lovell C. C., Waters D., 2017, MNRAS, 469, 2517
Wyithe J. S. B., Loeb A., 2011, MNRAS, 413, L38
Yung L. Y. A., Somerville R. S., Finkelstein S. L., Popping G., Davé R., 2019, MNRAS, 483, 2983
Yung L. Y. A., Somerville R. S., Popping G., Finkelstein S. L., Ferguson H. C., Davé R., 2019, MNRAS, 490, 2855

APPENDIX A: COMPARING DIFFERENT ISOCHRONE MODELS

We examine how the simulated UVLF and β–M_{1500} relation change with different isochrone models. Specifically, we run PYLOSER
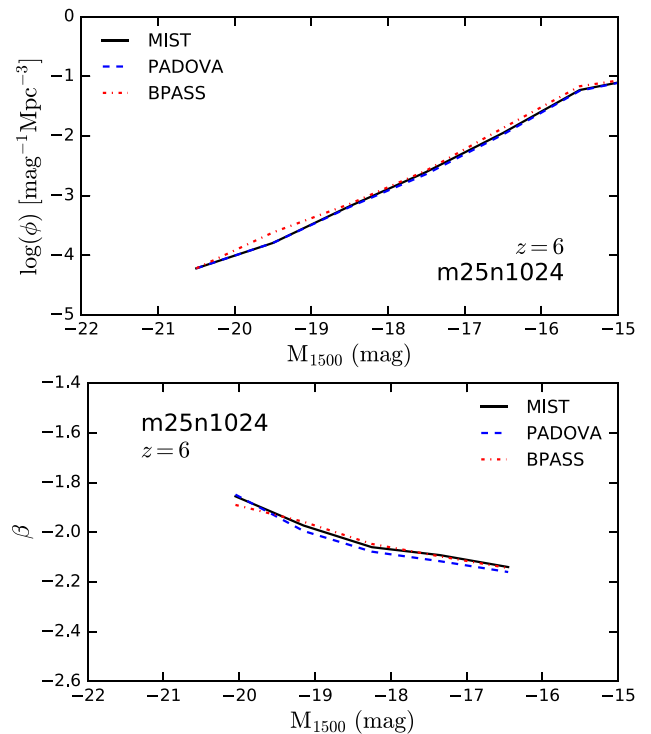

Figure A1. The UVLF (top) and β–M_{1500} relation (bottom) at $z = 6$ in SIMBA-25, computed using MIST + MILES (black solid lines), PADOVA + MILES (blue dashed lines), and BPASS (red dotted–dashed lines). The predictions on the far-UV spectrum are very similar among different models.

with three different combinations of isochrone model and spectral library implemented in FSPS: MIST + MILES, Padova + MILES, and the Binary Population and Spectral Synthesis (BPASS) model with pre-computed single stellar populations (Eldridge et al. 2017; Stanway & Eldridge 2018). Because the BPASS model assumes the Salpeter (1955) IMF, we run the other models with this IMF for better comparison. Nebular emission (pre-computed in FSPS) is also included. We perform this calculation only for the $z = 6$ galaxies in SIMBA-25.

Fig. A1 shows the UVLF (top panel) and β–M_{1500} relation (bottom panel) at $z = 6$ in SIMBA-25. Black solid, blue dashed, and red dotted–dashed lines represent MIST, PADOVA, and BPASS, respectively. The different model predictions on the UVLF and the β–M_{1500} relation are thus very similar. This is consistent with the findings of Choi et al. (2017) that the predictions on the far-UV spectrum by different isochrone models are very similar. It is only the ionizing photon production that differs a lot when changing the

isochrone models. Thus, the photometric properties of the simulated galaxies are robust with respect to changes in the isochrone model. This comparison also implies that altering an isochrone model cannot mitigate the disagreement between the simulated $z = 8$ UVLF and the observations.

This paper has been typeset from a TeX/LaTeX file prepared by the author.